Carbon concentration increases with melting depth in Earth's upper mantle

Alessandro Aiuppa[1,*], Federico Casetta[2], Massimo Coltorti[2],

Vincenzo Stagno[3] and Giancarlo Tamburello[4]

[1]*Dipartimento di Scienze della Terra e del Mare, Università di Palermo, Italy*

[2]*Dipartimento di Fisica e Scienze della Terra, Università di Ferrara, Italy*

[3]*Dipartimento di Scienze della Terra, Università di Roma La Sapienza, Italy*

[4]*Istituto Nazionale di Geofisica e Vulcanologia, Sezione di Bologna, Italy*

Carbon in the upper mantle controls incipient melting of carbonated peridotite and so acts as a critical driver of plate tectonics. The carbon-rich melts that form control the rate of volatile outflux from the Earth's interior, contributing to climate evolution over geological times. However, attempts to constrain the carbon concentrations of the mantle source beneath Oceanic Islands and Continental Rifts is complicated by pre-eruptive volatile loss from magmas. Here, we compile literature data on magmatic gases, as surface expression of the pre-eruptive volatile loss, from 12 Oceanic Island and continental Rift volcanoes. We find the levels of carbon enrichment in magmatic gases correlate with the trace element signatures of the corresponding volcanic rocks, implying a mantle source control. We use this global association to estimate that the mean carbon concentration in the upper mantle, down to 200 km depth, is approximately 350 ppm (range, 117-669 ppm). We interpret carbon mantle heterogeneities to reflect variable extents of mantle metasomatism from carbonated silicate melts. Finally, we find that the extent of carbon enrichment in the upper mantle positively correlates with the depth at which melting starts. Our results imply a major role of C in driving melt formation in the upper mantle.

Measuring the C concentration in mantle-sourced magmas[1-3] (Fig. 1) is, together with melting experiments[4-6] and the recovery of mantle-derived diamonds[7] and xenoliths[8], the main way to assess the C-rich nature of the Earth's mantle. However, owing to limited solubility in silicate melts under crustal conditions, erupted magmas are extensively depleted in C by degassing, to the point that even the most deeply trapped melt inclusions (MIs) in crystals fail to record the initial (mantle-inherited) C cargo[9]. Thus, while consensus exists that the majority of C on Earth is deeply stored[10-11], the mantle C budget remains a matter of debate[12-14].

To correct for pre- and post-entrapment gas loss to bubbles[15-16] and therefore estimate the initial C content of parental melts and their mantle sources, geochemists pair CO_2 in MIs with incompatible (and nonvolatile) trace elements[13,17] that behave similarly to C during partial melting, such Nb and Ba (Fig. 1b-c). Reconstructing the mantle CO_2/Ba ratio[2,13] (Fig. 1c) from analysis of rare undegassed MIs[2,18] and glasses[19] in mid-ocean ridge basalts (MORBs) has constrained the average C content of the depleted MORB mantle (DMM) at ~20-56 ppm[1,20]. However, the wide inter-ridge variability[20] (range 3-540 ppm C) implies an heterogeneous[2] DMM, with the highest C contents in MOR segments near active hot spots[20] suggesting a more C-rich deeper mantle.

The C content of deeper regions of the convecting mantle can potentially be traced by plume-related mid-ocean ridges (e.g., Iceland[21]), Oceanic Island Basalts (OIBs; ref. 16,22-26) and Continental Rift (CR) magmas[27], as these melts are extracted from deeper (>50 km) sources than MORBs. However, the C-enriched signature[1,16] of OIBs cause their volatile saturation deep in the crust/mantle, making MIs often degassed[24-26] (Fig. 1b). The case is even more exacerbated in CR setting, where the prevailing silica-undersaturated alkaline erupted magmas imply a metasomatised C-rich mantle source[27], but even the most CO_2-rich (up to ~ 1 wt%) MIs[28-29] are affected by pre-entrapment C-loss (Fig. 1b, c). Nevertheless, a better knowledge of the C content in mantle sources underneath rifting cratons[27] is vital to modelling the deep C cycle[30-34].

Carbon that is lost to vapour during decompression-driven magma degassing, while predominantly escaping the MI record, can be directly quantified by measuring the shallow release of magmatic gas CO_2 through fumaroles and plumes during both volcano quiescence and eruption[31]. Considering the low residual volatile contents in erupted magmas[9], the magmatic gas output corresponds to the total volatile budget of the magma batch under the condition that closed-system degassing has prevailed during ascent, followed by near-surface gas-melt separation (as observed at mafic volcanoes[35-36]). In worldwide subduction-zone volcanoes[37-38] for example, the abundance of CO_2 scaled to more magma-soluble sulphur S (i.e., the CO_2/S_T ratio, where $S_T = SO_2 + H_2S$) correlates with the trace element slab-fluid proxies in magmas, implying an essential control exerted by the volatile signature of the source mantle wedge[39].

Non-arc (e.g., MOR, OIB and CR-related) magmatic gases are typically richer[40] in CO_2 compared with their arc counterparts[37], with extreme CO_2 enrichments observed in gas released by alkaline magmatic systems of the East African Rift (EAR), where the source mantle is expected to retain high C amounts[27]. However, the link between C-rich magmatic gases and their mantle source characteristics has not been quantitatively explored.

Magmatic gas compositions and parental melt C contents

There are only 12 volcanoes in plume-related (MOR and intraplate) and CR settings for which high-temperature (>450 °C) gas composition information is available (see Extended Data Fig. 1-2 and Extended Data Table 1-2 for location and data provenance). For this volcano selection, we illustrate in Fig. 2 a,b (and Extended Data Fig. 3) the relationship between the time-averaged (mass) magmatic gas CO_2/S_T ratios and the trace element compositions of the corresponding volcanic rocks (see Methods). Among these, we focus on Sr, Nd, and Sm whole-rock ratios because these elements exhibit similar behaviour (i.e., similar incompatibility) during magma generation in the mantle. Thus, the spread of Sr/Sm and Sr/Nd ratios cannot be explained either by variable degrees of

76 melting of the same mantle source or by different degrees of magma differentiation (Extended Data
77 Fig. 4).
78 Indeed, the resulting correlations (Figs. 2a,b) suggest that (i) OIB and CR gases are C-enriched
79 (relative to S_T) compared to the composition of the DMM, and (ii) the level of such C enrichment
80 scales with the extent of enrichment in Sr (and other large ion lithophile elements, LILEs) in the
81 source magmas.
82 Ratios between incompatible/nonvolatile LILEs and light rare earth elements (LREE), which are
83 unaffected by magma differentiation/degassing upon ascent and crustal emplacement (Extended
84 Data Fig. 4), are typically used to constrain the enriched/depleted nature of their mantle sources
85 [37,41]. Thus, the correlations in Fig. 2a-b ultimately imply that the magmatic gas CO_2/S_T ratios are
86 also controlled by source mantle characteristics, e.g., that degassing-driven fractionation has little
87 control on time-averaged gas compositions[37]. The corollary is that magmatic gas CO_2/S_T ratios may
88 serve as proxies to estimate the parental C content in both undegassed magmas and the source
89 mantle.
90 For each of the 12 volcanoes we convert the CO_2/S_T ratios into parental melt C contents (Fig. 1) by
91 multiplying by the corresponding parental melt S contents. The latter are inferred from the measured
92 S contents (0.07 to 0.37 wt. %; Extended Data Table 1) in the most mafic (e.g., primitive) olivine-
93 hosted MIs for each volcano. Being generally entrapped at relatively high pressure (> 100 MPa),
94 these MIs have escaped S loss to gas[9]. Our inferred parental melt CO_2 contents range from 0.12 to
95 6.2 wt% (Extended Data Table 3), increase with magma alkalinity and are systematically higher
96 than (or, in a few cases, at the upper range of) those measured in MIs (Fig. 1a,b). This mismatch,
97 and especially the fact that our gas-derived CO_2 contents convert into CO_2/Ba and CO_2/Nb within
98 the mantle range (Figs 1b, c), while MI-based CO_2 contents do not, provides confidence in our
99 magmatic gas-based methodology and confirms that MIs are in most cases extensively degassed
100 (and C depleted relative to nonvolatile Ba and Nb; ref. 1-3).

Our results constrain the CO_2 transport capacity of CR magmas at 1-6 wt%, within the range of parental melt CO_2 contents (of 3–24 wt%) predicted on the basis of CO_2/trace element ratios in MIs from EAR magmas[29]. We emphasise that while correcting MIs for pre-entrapment CO_2 loss[1] requires a priori assumptions on the source CO_2/trace element proxy ratio (which may vary in a heterogeneous mantle[2]), our method does not. We also infer parental melt CO_2 contents of 0.12-1.1 wt% for plume-related tholeiitic magmas, with the lower and upper ranges being consistent with recent independent estimates for Iceland[21] and Hawaii[22], respectively (Extended Data Table 3).

Mantle C contents

We next infer the C content of the mantle sources underneath the 12 volcanoes (Fig. 3 and Extended Data Table 3) by applying a batch-melting equation (see Methods) to our derived parental melt CO_2 contents and using estimated mantle melting fractions (F) for each locality (listed in Extended Data Table 3). As disparate and often limited information exists for mantle source characteristics (mineral modal abundances and chemical composition), we cautiously determine F for each of the 12 volcanoes from modelling Zr partitioning between primitive melts and two possible end-member mantle sources (primitive and enriched mantle; see Methods).

Our best-estimated F values range from 0.03 (Erebus) to 0.18 (Piton de la Fournaise) (Extended Data Table 3). From these, and the parental melt C contents, we infer C contents in the mantle sources ranging between 117 and 669 ppm (Extended Data Table 3). Our results unambiguously demonstrate that, as recently suggested[12,22,42], mantle sources sampled by OIB and CR magmas are systematically C-richer than the "averaged" DMM (20-56 ppm C, ref. 1,20,43). If deeper (than normally sampled by MORBs) portions of the convecting mantle are C-rich, then the few C-enriched DMM segments[20] that plot within the OIB/CR range (Fig. 3) must result from lateral transport of enriched plume-related melts towards ridges[44].

In Fig. 3, our estimated mantle C contents positively correlate with the pressure of initiation of mantle melting, as derived from using a P-dependent, H_2O-independent barometer (see Methods).

Our results thus identify a downward C increasing trend in the mantle source of OIB and CR magmas (Fig. 3). We stress that the "mantle source" we here refer to corresponds to the region of mantle melting and magma formation that, especially in the case of OIB, is shallower than the initial source area of mantle plumes (which are typically rooted in the deep mantle).

We integrate the inferred C vs. depth dependence ($[C_{,ppm}] = 330 \cdot \ln(depth_{,km}) - 1120$; Fig. 3) down to 200 km depth to estimate that the mantle melting regions that source OIB and CR magmas (Fig. 3) contain ~$1.2 \cdot 10^{23}$ g C (confidence interval, 0.95 to $1.4 \cdot 10^{23}$ g). Extrapolating the same function to depths > 200 km is geochemically less constrained owing to the lack of recently erupted lavas originating from such deep mantle sources and because redox freezing potentially limits deeper infiltration of subducted carbonates[45]. Our calculations indicate that the upper (< 200 km) mantle contains ~352 ppm C on average (confidence interval, 284 to 419). We conclude that the average mantle C concentration exceeds that predicted (110±40 ppm C) using CO_2/Ba systematics of minimally degassed magmas[13] and is more likely within the range obtained using the nitrogen terrestrial budget[12] (337-479 ppm C). Recent mantle C estimates from OIBs (201-344, ref. 22; 368 ppm C, ref. 42) also match our estimate closely.

Modelling the C vs. trace element association.

Our parental melt/source mantle C estimates are based on the assumption that the consistent and parallel enrichments in C and LILEs (relative to DMM) observed in plume-related (Iceland and OIBs) and CR magmas (Fig. 2) are source controlled. There are obvious potential drawbacks to this approach. For example, the magma CO_2/S_T budget can be potentially altered by interaction with crustal C-rich rocks[37]. However, chemical and isotopic tracers (Sr-Nd-Pb-C) indicate that assimilation of C-rich crustal lithotypes is negligible (if any) at most of our selected volcanoes (Supplementary Information). We cannot exclude that at volcanoes overlying sedimentary successions (e.g., Etna), a minor CO_2 fraction is derived from de-carbonatation reactions of crustal limestones[37]. However, our CO_2 vs. Nb-Ba (Fig. 1) and Sr (Fig. 4) relationships rule out the

possibility that crustal limestones are major C sources that impact the gas CO_2/S_T ratio. Modelling also shows that sulphide saturation in magmas has little control on magmatic gas CO_2/S_T (Supplementary Information). We conclude, therefore, that the C-LILE/REE association (Fig. 2) reflects their common derivation from a fertile (C-rich) source.

Experimental and petrological evidence suggests that the most common C-LILE carriers and metasomatic agents[46] in the mantle are C-rich melts[6], formed via incipient melting of either carbonated peridotites[4-5] and/or subducted carbonated oceanic crust[47]. Such incipient mantle melts form a continuous trend from carbonatitic to carbonated silicate (kimberlite-like) melts[4-6], and erupted carbonatitic (Cb) to kimberlitic (Kb) rocks thus represent their best surface-emplaced analogues. These rocks are C-rich and have high Sr/Nd and Sr/Sm ratios (Fig. 4 and Extended Data Fig. 5), and mantle metasomatism via carbonatitic/kimberlitic melts is therefore a suitable mechanism to explain our CO_2/S_T vs. Sr/LREE association (Fig. 2). We therefore back-process our gas vs. trace element data (Fig. 2) (i) to test whether the compositional trends exhibited by the 12 volcanoes correspond to those of mantle-derived melts formed by a suite of mantle sources variably enriched in C and LILE and (ii) to verify whether the mantle enrichment process is consistent with the addition, to a DMM-like mantle, of small amounts of metasomatic C-rich melts (mCm), an analogue of natural kimberlitic (Kb) to carbonatitic (Cb) (Fig. 4, Extended Data Fig. 5) melts, and (iii) to derive the trace element signature of these mCm by data regression.

The procedure (see Methods) involves calculation of $(CO_2/S_T)_M$ and $(Sr/X)_M$ ratios (where X is a given trace element; Extended Data Fig. 6) of the mantle sources (M) at equilibrium with the original volcanic gas vs. rock dataset (Fig. 2). This was obtained by applying a batch-melting equation and using a range of melting fractions F (0.025, 0.5, 0.1, 0.2) covering the mantle melting conditions observed at the studied volcanoes (Extended Data Table 3). Then, the obtained $(CO_2/S_T)_M$ and $(Sr/X)_M$ ratio population was fitted using a best-fit mixing equation (see Methods; Extended Data Fig. 6). This data regression is initialised with a set of assigned C, S, and Sr values for the mCm (Extended Data Table 4) based on the composition of natural kimberlitic and

carbonatitic rocks and/or experimental melts[4-6] (Fig. 4, Extended Data Fig. 5). From this, the whole trace element compositional suite of the mCm is obtained by regression (Extended Data Table 4 and Fig. 5). We consider five distinct model scenarios (Cb1, Cb2, Kb1, Kb2, and Kb3) to cover the possible C, S, and Sr mCm ranges (see Methods).

The results (Fig. 5a,b) show that our model curves well match the gas (CO_2/S_T) vs. trace element global populations. Therefore, partial melting of a suite of variably C-LILE-enriched mantle sources derived from 0.01-0.1 wt% (tholeiites) to 0.1-2.0 wt% (alkaline CR magmas) mCm addition to the DMM is a suitable mechanism to explain the global C-LILE enrichment pattern (Figs. 1,4-5 and Extended Data Fig. 5). The derived primordial mantle (PM)-normalised trace element compositions of our mCms share high chemical affinity with natural (erupted) kimberlites (Fig. 5c), suggesting that carbonated silicate melts (rather than carbonatitic melts) are the most likely metasomatic fluids in the mantle. Carbonatitic[47] and kimberlitic[48] melts have both been found trapped in sub-lithospheric diamonds and, thus, are associated with metasomatic fluids permeating the lower portion of the upper mantle. The stability of these CO_2(-H_2O)-bearing fluids is linked to P-T-fo_2 conditions required for melting of diamond-bearing peridotites to occur. For a lithospheric mantle whose redox state decreases with depth[49], kimberlitic melts (approximately 10-20 wt% CO_2; our Kb1 and Kb2 modelled compositions) would form in equilibrium with a diamond-bearing source at $-3 \leq fo_2$ (ΔFMQ) ≤ -2 log units[49].

Our results provide compelling evidence for the role of mCm in determining the C-LILE heterogeneity of the Earth's upper mantle (Figs. 5-6). Even more importantly, the dependence between mantle C content and depth/pressure on initiation of melting we bring to light (Fig. 3) provides independent observational confirmation for the experimentally determined[4-5] role of C in driving melting in the mantle. It has been experimentally demonstrated[4-5] that trace C in the upper mantle forces mantle peridotites to start melting significantly deeper than would occur in volatile-free conditions. It has been argued, in particular, that 0.1-1 wt% carbonated silicate melts can form at 100-250 km depth in a moderately wet (0-200 ppm H_2O) carbonated mantle containing 27-81

ppm C (ref. 4). Our results (Fig. 3) provide evidence for C-rich mantle regions melting deeper than DMM. If, as our data suggest, the Earth's mantle contains ~400 to ~700 ppm C in the 100-250 km mantle window (Fig. 3), then C-induced incipient melting of carbonated peridotite may advance to melt fractions higher (even by two orders of magnitude) than previously thought[5]. If we assume, for instance, that incipient melts that form are kimberlite-like magmas with 10 to 20 wt% CO_2 (ref. 4-5), then a 400-700 ppm mantle C range would imply melting fractions of 0.7-2.6 wt%. Redox melting may also play a major role, provided redox conditions required to oxidise a diamond-bearing mantle source ($Fe^{3+}/\sum Fe >> 4\%$) persist. Indeed, the addition of C to an Fe^{3+}-rich mantle source would cause the onset of (redox) melting at much deeper conditions[49]. Upon ascent, the so-formed carbonated silicate melts may thus exert a key control on the mineralogical[46] and chemical[41] heterogeneity of the overlying mantle, sampled by OIBs and MORBs (Fig. 6). If mCms are the main C carrier in the deep upper mantle (Figs. 4-6), then their limited transport capacity in the shallow lithospheric mantle may ultimately control the C downward trend (Fig. 3). The C-rich mantle our results evoke, and the incipient melting that (in combination with H_2O) this C would lead to, may also well explain[1,2,4] the geophysical anomalies in the upper mantle that, to be observable, would require higher melt fractions. Ultimately, our results emphasise the central role C plays in driving the geodynamics and long-term evolution of our planet.

Data availability

All data generated or analysed during this study are included in this published article (Extended Data Tables 1-4). The dataset is also publicly available in the Earthchem data repository (https://www.earthchem.org/ecl/).

Code availability

The code that supports the findings of this study and used to generate Figs. 1,5 and Exstended Data Fig. 6 is available from author Giancarlo Tamburello (giancarlo.tamburello@ingv.it) upon request.

References cited

1. Hauri, E.H. et al., Carbon in the convecting mantle, In: Deep Carbon, Past to Present, Edited by B.N. Orcutt, I. Daniel, and R. Dasgupta. Cambridge University Press, 237-275, www.cambridge.org/9781108477499, doi: 10.1017/9781108677950 (2020)
2. Le Voyer, M., Kelley, K.A., Cottrell, E., & Hauri, E.H. Heterogeneity in mantle carbon content from CO_2-undersaturated basalts. *Nat. Comm*. **8**, 14062 (2017).
3. Saal, A.E., Hauri, E.H., Langmuir, C.H., & Perfit, M.R. Vapour undersaturation in primitive mid-ocean-ridge basalt and the volatile content of Earth's upper mantle. *Nature* **419**, 451–455 (2002).
4. Dasgupta, R., Mallik, A., Tsuno, K., Withers, A. C., Hirth, G. & Hirschmann M. M. Carbon-dioxide-rich silicate melt in the Earth's upper mantle. *Nature* **493**, 211–215 (2013).
5. Dasgupta, R. Volatile-bearing partial melts beneath oceans and continents – where, how much, and of what compositions? *Am. J. Sci*. **318**, 141–165 (2018).
6. Yaxley, G.M., et al., CO_2-rich melts in Earth, In: Deep Carbon, Past to Present, Edited by B.N. Orcutt, I. Daniel, and R. Dasgupta. Cambridge University Press, 129-162, www.cambridge.org/9781108477499, doi: 10.1017/9781108677950 (2020)
7. Shirey, S.B., et al. Diamonds and Mantle geodynamics of Carbon, In: Deep Carbon, Past to Present, Edited by B.N. Orcutt, I. Daniel, and R. Dasgupta. Cambridge University Press, 89-128, www.cambridge.org/9781108477499, doi: 10.1017/9781108677950 (2020)
8. Pearson, D.G., Canil, D., & Shirey, S.B. Mantle Samples Included in Volcanic Rocks: Xenoliths and Diamonds, In Treatise on Geochemistry, The Mantle and Core, (ed. Carlson, R.W.), Elsevier, Second Edition 4, 169-253, (2014).
9. Wallace, P.J., Plank, T., Edmonds, M. & Hauri, E.H. Volatiles in Magmas. In The Encyclopedia of Volcanoes (Second Edition). (eds. Sigurdsson, H., Houghton, B., McNutt, S., Rymer, H. and Stix, J.). Academic Press, Elsevier, 163-183 (2015).

10. Javoy, M., Pineau, F. & Allegre, C.J. Carbon geodynamic cycle. *Nature*, **300**, 171–173, https://doi.org/10.1038/300171a0 (1982).

11. Dasgupta, R., & Hirschmann, M.M. The deep carbon cycle and melting in Earth's interior. *Earth Planet. Sci. Lett.* **298**, 1–13 (2010).

12. Marty, B., Almayrac, M., Barry, P.H., Bekaert, D.V., Broadley, M.W. Byrne, D.J., Ballentine, C.J., Caracausi, A., An evaluation of the C/N ratio of the mantle from natural CO_2-rich gas analysis: Geochemical and cosmochemical implications- *Earth Planet. Sci. Lett.* **551**, (2020).

13. Hirschmann, M.M. Comparative deep Earth volatile cycles: the case for C recycling from exosphere/mantle fractionation of major (H_2O, C, N) volatiles and from H_2O/Ce, CO_2/Ba, and CO_2/Nb exosphere ratios. *Earth Planet. Sci. Lett.*, **502**, 262–273 (2018).

14. Stagno, V., Cerantola, V., Aulbach, S., Lobanov, S., McCammon, C.A., Merlini, M.. Carbon-bearing phases throughout Earth's interior - evolution through space and time. In B. Orcutt, I. Daniel, & R. Dasgupta (Eds.), Deep Carbon: Past to Present (pp. 66-88). Cambridge: Cambridge University Press (2019).

15. Moore, L. R., Gazel, E., Tuohy, R., Lloyd, A. S., Esposito, R., Steele-MacInnis, M., Hauri, E. H., Wallace, P. J., Plank, T. & Bodnar R. J. Bubbles matter: An assessment of the contribution of vapor bubbles to melt inclusion volatile budgets. *Am. Mineral.*, **100**, 806–823 (2015).

16. Tucker, J.M. et al., A high carbon content of the Hawaiian mantle from olivine-hosted melt inclusions. *Geochim. Cosmochim. Acta,* **254**, 156–172 (2019).

17. Rosenthal, A., Hauri, E. H. & Hirschmann, M. Experimental determination of C, F, and H partitioning between mantle minerals and carbonated basalt, CO_2/Ba and CO_2/Nb systematics of partial melting, and the CO_2 contents of basaltic source regions. *Earth Planet. Sci. Lett.*, **425**, 77–87 (2015).

18. Le Voyer, M. et al., Carbon fluxes and primary magma CO_2 contents along the global mid-ocean ridge system. *Geochem. Geophys. Geosyst*. **20**, 1387–1424 (2019).

19. Michael, P. J. & Graham, P. J. The behavior and concentration of CO_2 in the suboceanic mantle: inferences from undegassed ocean ridge and ocean island basalts. *Lithos,* **236–237**, 338–351 (2015).

20. Cottrell, E., Kelley, K.A., Hauri, E.H., & Le Voyer, M., Mantle Carbon Contents for Mid-Ocean Ridge Segments. Interdisciplinary Earth Data Alliance. doi:10.1594/IEDA/111333 (2019).

21. Hauri, E.H. et al., CO_2 content beneath northern Iceland and the variability of mantle carbon. Geology, 46, 55–58 (2017)

22. Anderson, K.R., & Poland, M.P. Abundant carbon in the mantle beneath Hawai'i. *Nature Geosci*., **10**., 704-708 https://doi.org/10.1038/NGEO3007 (2017).

23. Boudoire, G., Rizzo, A.L., Di Muro, A., Grassa, F., Liuzzo, M., Extensive CO_2 degassing in the upper mantle beneath oceanic basaltic volcanoes: First insights from Piton de la Fournaise volcano (La Réunion Island). *Geochim. Cosmochim. Acta* **235,** 376-401 (2018)

24. Bureau, H., Pineau, F., Metrich, N., Semet, M.P. & Javoy, M. A melt and fluid inclusion study of the gas phase at Piton de la Fournaise volcano (Reunion Island). *Chem. Geol*. **147**, 115–130 (1998).

25. Métrich, N. et al., Is the "Azores Hotspot" a wetspot? Insights from the geochemistry of fluid and melt inclusions in olivine of Pico basalts. *J. Petrol*. **55**, 377–393 (2014).

26. Longpré, M.-A., Stix, J., Klügel, A., & Shimizu, N., Mantle to surface degassing of carbon- and sulphur-rich alkaline magma at El Hierro, Canary Islands. *Earth Planet. Sci. Lett*. **460**, 268–280 (2017)

27. Foley, S.F., & Fischer, T.P. An essential role for continental rifts and lithosphere in the deep carbon cycle. *Nature Geosci.*, **10**, 897-902 https://doi.org/810.1038/s41561-41017-40002-41567. (2017).

306 28. de Moor, J.M., et al., Volatile-rich silicate melts from Oldoinyo Lengai volcano (Tanzania):
307 Implications for carbonatite genesis and eruptive behaviour. *Earth Planet. Sci. Lett.*, **361**, 379–
308 390 (2013)
309 29. Hudgins, T.R., et al., Melt inclusion evidence for CO_2-rich melts beneath the western branch
310 of the East African Rift: implications for long-term storage of volatiles in the deep lithospheric
311 mantle. *Contrib Mineral Petrol,* **169**: 46 (2015)
312 30. Lee, H., Muirhead, J.D., Fischer, T.P., Ebinger, C.J., Kattenhorn, S.A., Sharp, Z.D. &
313 Kianji, G., Massive and prolonged deep carbon emissions associated with continental rifting.
314 *Nat. Geosci*., DOI: 10.1038/NGEO2622 (2016).
315 31. Werner, C., et al., Carbon Dioxide Emissions from Subaerial Volcanic Regions: Two
316 Decades in Review. In: Deep Carbon, Past to Present, Edited by B.N. Orcutt, I. Daniel, and R.
317 Dasgupta, 188-236, Cambridge University Press, www.cambridge.org/9781108477499, doi:
318 10.1017/9781108677950 (2020)
319 32. Muirhead, J.D., Fischer, T.P., Oliva, S.J. et al. Displaced cratonic mantle concentrates deep
320 carbon during continental rifting. *Nature*, **582**, 67-72 (2020)
321 33. Brune, S., Williams, S.E. & Muller, R. D. Potential links between continental rifting, CO_2
322 degassing and climate change through time. *Nat. Geosci*. **10**, 941–946 (2017).
323 34. Tappe, S., Smart, K.A, Torsvik, T.H., Massuyeau, M., de Wit M.C.J. Geodynamics of
324 kimberlites on a cooling Earth: Clues to plate tectonic evolution and deep volatile cycles. *Earth*
325 *Planet. Sci. Lett.*, **484**, 1-14. doi:10.1016/j.epsl.2017.12.013 (2018)
326 35. Aiuppa, A., Moretti, R., Federico, C., Giudice, G., Gurrieri, S., Liuzzo, M., Papale, P.,
327 Shinohara, H. & Valenza, M. Forecasting Etna eruptions by real-time observation of volcanic
328 gas composition. *Geology,* **35** (12), 1115-1118 (2007).
329 36. Edmonds, M. New geochemical insights into volcanic degassing. *Phil. Trans. R. Soc. A*, **366**
330 (1885), 4559-4579 (2008).

37. Aiuppa, A., Fischer, T. P., Plank, T., Robidoux, P. & Di Napoli, R. Along-arc, interarc and arc-to-arc variations in volcanic gas CO_2/S_T ratios reveal dual source of carbon in arc volcanism. *Earth Science Reviews,* **168**, 24–47 (2017)

38. Aiuppa, A., Fischer, T.P., Plank, T. & Bani, P. CO_2 flux emissions from the Earth's most actively degassing volcanoes, 2005–2015. *Sci. Reports*, **9**:5442 | https://doi.org/10.1038/s41598-019-41901-y (2019).

39. Plank, T., & Manning, C.E., Subducting Carbon. *Nature*, **574**, 343–352 https://doi.org/10.1038/s41586-019-1643-z (2019).

40. Gerlach, T.M. (1982), Interpretation of volcanic gas data from tholeiitic and alkaline mafic lavas, *Bull. Volcanol*., **45**, 235–244.

41. Zindler, A. & Hart, S., Chemical geodynamics. *Ann. Rev. Earth Planet. Sci*. **14**, 493–571 (1986).

42. Miller, William GR, Maclennan, J., Shorttle, O., Gaetani, G.A., Le Roux, V., Klein, F., Estimating the carbon content of the deep mantle with Icelandic melt inclusions. *Earth Planet. Sci. Lett* **523,** 115699 (2019).

43. Bekaert, D.V., Turner, S.J., Broadley, M.W., Barnes, J.D., Halldórsson, S.A., Labidi, J., Wade, J., Walowski, K.J., Barry P.H., Subduction-Driven Volatile Recycling: A Global Mass Balance. *Annu. Rev. Earth Planet. Sci*. **49**, 37–70 (2021).

44. Gibson, A.A., Richards, M.A., Delivery of deep-sourced, volatile-rich plume material to the global ridge system, *Earth Planet. Sci. Lett*. **499**, 205–218 (2018).

45. Rohrbach, A. & Schmidt, M.W. Redox freezing and melting in the Earth's deep mantle resulting from carbon–iron redox coupling. *Nature*, **472**, 209–212 (2011).

46. O'Reilly, S.Y., & Griffin, W. Mantle metasomatism, In Metasomatism and the Chemical Transformation of Rock (Eds, Harlov, D.E., Austrheim, H), 471-533, Springer-Verlag Berlin Heidelberg (2013)

47. Walter, M.J. et al. Primary carbonatite melt from deeply subducted oceanic crust. *Nature* **454**, 622–625 (2008).

48. Smith, E.M., Kopylova, M.G., Nowell, G.M., Pearson, D.G. & Ryder, J. Archean mantle fluids preserved in fibrous diamonds from Wawa, Superior Craton. *Geology* **40**, 1071–1074 (2012).

49. Stagno, V., Ojwang, D.O., McCammon, C.A. & Frost, D.J. The oxidation state of the mantle and the extraction of carbon from Earth's interior. *Nature*, **493**, 84–88 (2013).

50. Cartigny, P., Pineau, F., Aubaud, C., & Javoy, M., Towards a consistent mantle carbon flux estimate: insights from volatile systematics (H_2O/Ce, δD, CO_2/Nb) in the North Atlantic mantle (14°N and 34°N). *Earth Planet. Sci. Lett*. **265**, 672–685 (2008).

Corresponding author

Correspondence to: Alessandro Aiuppa (alessandro.aiuppa@unipa.it)

Acknowledgements

This work received funding from the Deep Carbon Observatory (subcontract no. 10759-1238; A.A.) and from the Italian Ministero Istruzione Università e Ricerca (Miur, Grant N. 2017LMNLAW; A.A.). The funders had no role in study design, data collection and analysis, decision to publish or preparation of the manuscript. We thank A. Rohrbach for useful comments on an earlier version of the manuscript.

Author contribution

A.A. devised the study concept. A.A., F.C., M.C., V.S. and G.T. contributed to refinement of the initial concept, and to data analysis and interpretation. A.A. drafted the original version of the manuscript with contributions from all coauthors.

Competing Interests Statement

The authors declare no competing interests.

Figure Captions

Figure 1 – CO_2 contents in mafic melts from plume-related and Continental Rift volcanoes. Our estimated parental melt CO_2 contents (Extended Data Table 3) are shown on the vertical axis, as determined by combining measured volcanic gas CO_2/S_T ratios with S contents in primitive MIs. **(a)** The calculated parental melt CO_2 contents are plotted against measured CO_2 contents in MIs in the same volcanoes (x-scale), where available; the latter, being systematically lower, imply extensive CO_2 loss prior to/after MI entrapment. The derived CO_2 content of Ol Doinyo Lengai overestimates the real parental melt CO_2 (the gas compositions used include low-temperature gases where S has been scrubbed; see Extended Data Table 1). The measured Ardoukoba gas is a residual (CO_2-depleted) gas (Extended Data Table 1); as such, we instead use the CO_2/S_T ratio inferred from the gas-trace element relationship (Fig. 2): $[(CO_2/S_T)_i = 0.35 \cdot \exp(0.03 \cdot (Sr/Sm)_m))$. The same equation is used to calculate parental melt CO_2 contents for the Laki and Nabro eruptions, for which no volcanic gas data exist. **(b)** Nb vs. CO_2 plot, in which the majority of the "degassed" MIs plot below (at lower CO_2/Nb ratios lower than) the CO_2-Nb mantle array (grey area), as defined by undegassed MORB MIs and glasses (characteristic upper mantle CO_2/Nb ratios are from ref. 2,3,13,50). Our inferred parental melt CO_2 contents, when plotted in tandem with measured Nb contents in primitive MIs or whole/rocks (Extended Data Table 1), extend the mantle array to more C-Nb enriched compositions; stars indicate the derived composition of kimberlitic (Kb) to carbonatitic (Cb) metasomating C-rich melts (mCms), see text; **(c)** same as (b), but using Ba in primitive MIs or whole/rocks as trace element proxy. Our parental melt CO_2-Ba population falls within the CO_2/Ba mantle range (74-120). In (b) and (c) the compositional field of crustal limestones is from ref. 37.

Figure 2 – Time-averaged volcanic gas CO_2/S_T ratios vs. mean whole-rock Sr/Sm and Sr/Nd ratios. Scatter plots contrasting, for the 12 volcanoes, the time-averaged volcanic gas CO_2/S_T ratios with the corresponding mean whole-rock Sr/Sm and Sr/Nd ratios (Extended Data Table 1). The best-fit regression lines (with equations and regression coefficients) are shown in red. The averaged volatile composition of the DMM is calculated by combining data in ref. 1,3,18,20.

Figure 3 – C contents in the source mantles of plume-related (OIB and Iceland) and Continental Rift volcanoes. C contents (Extended Data Table 3) derived by applying a batch-melting equation to the parental melt CO_2 contents and using an appropriate melting fraction (F) for each volcano (Extended Data Table 3 and Methods). For each volcano, the symbol identifies our best-estimated C content (the horizontal bar identifies the possible range for the possible F range), and is plotted against pressure/depth of initiation of melting (Methods). The C vs. depth population was fit by data regression (we also included the C= 20 ppm mode[20] of the C frequency distribution in the DMM in the data fit). This identifies a downward increase in C concentrations in the upper mantle (equation shown with 2.5% and 97.5% confidence intervals). Our inferred melting depth vs. C dependence is statistically significant, as a one-tailed Spearman test yields a p-value of 0.0004848 (e.g., there is <5% probability that the two variables are uncorrelated).

For comparison, we also show the mantle C contents for 711 individual MOR segments[20] and for some plume-related OIB volcanoes (see legend, parental melt CO_2 contents from ref. 1 were converted into source mantle C using the batch melting equation and inferred melting fractions; see Extended Data Table 3 for data sources).

Figure 4 - The composition of natural carbonatites and kimberlites. These are used to constrain the C, S and Sr composition of our metasomatic C-rich melts (mCm) Cb1-2 to Kb1-3. (**a**) CO_2 vs. Sr global distribution of natural carbonatitic and kimberlitic rocks (source GeoRoc; http://georoc.mpch-mainz.gwdg.de/georoc/). These define a compositional array overlapping (but

extending to more enriched compositions) the compositional array exhibited by our parental CO_2 (inferred, Fig. 1 and Extended Data Table 3) vs. Sr trend for the 12 selected volcanoes. The high correlation exhibited by the latter supports the accuracy of our estimated parental CO_2 contents. The best fit equation (regression coefficient shown in figure) is used to extrapolate the Sr concentrations at 20 and 40 wt. % CO_2, used for our mCm in all scenarios (except Cb1). MORBs and DMM plot at less enriched (C-Sr-poorer) compositions. The compositional field of crustal limestones[37] is also shown. (**b**) Derived Sr/Sm and Sr/Nd ratios for the 5 mCm. Sm and Nd are derived from data regression (see Methods). Similar Sr/Sm and Sr/Nd ratios are obtained in the 5 model scenarios explored.

Figure 5 – Modelling the gas-rock association. The volcanic gas CO_2/S_T ratio vs. (**a**) Sr/Sm and (**b**) Sr/Nd ratio global association (same as Fig. 2) compared with the results of the melting/mixing model. Our OIB/CR volcanoes identify a compositional array that spreads between the C-Sr-poor MORB and DMM (see legend for data sources; grey diamonds are from the GeoRoc MORB pre-compiled file; http://georoc.mpch-mainz.gwdg.de/georoc/) and a C-Sr-rich end-member. This trend is inconsistent with variable degrees of melting of the same DMM mantle source (see the DMM melting line). We interpret our OIB/CR array as being due to melting (melting fractions F shown) of a heterogeneous C-LILE-enriched mantle source formed by small additions (mixing fractions X, shown in red) of metasomatic C-rich melts (mCms; Cb1 and Kb1) to the DMM. The composition of these mCms is estimated by applying a nonlinear least-squares procedure to the gas/whole-rock population (see Methods). By sequentially applying the same procedure to a set of trace element ratios, the entire suite of trace elements is derived for the mCms, as shown in (**c**). This spider diagram compares the inferred primitive mantle (PM)-normalised trace element composition of the C-rich metasomatic melts (mCm) (Extended Data Table 4) with the composition of natural carbonatitic and kimberlitic melts (mean compositions of GeoRoc precompiled files; http://georoc.mpch-mainz.gwdg.de/georoc/). For clarity, only two models (Cb1 and Kb1) are

460 shown, although additional scenarios are also explored (see Fig. 4 and Methods). For each of the 2
461 models, the mean (circles) and range (min/max; shaded red and white areas) are indicated.
462
463 **Figure 6 – Schematic representation of the vertical distribution of carbon in the upper mantle**.
464 East-to west transect from the Middle Atlantic Ridge (A) to the Java volcanic arc in the Sunda arc
465 (B) (the inset on the upper right shows the trace of the AB cross-section). The cross-section shows a
466 schematic representation of the vertical distribution of carbon in the upper mantle, as inferred from
467 the [C] vs. depth relationship of Fig. 3. Mantle C contents below specific volcanoes and ridge
468 segments are from this study and ref. 20, respectively. The structure and thickness on the Sub-
469 Continental Lithospheric Mantle are only for illustrative purposes, and are meant to highlight the
470 development of a C-enriched, metasomatised mantle source underneath the African Craton, leading
471 to C-enriched EAR volcanism upon continental rifting[27,32]. The downward increasing C in the upper
472 mantle reflects C extraction from the shallow DMM as well as variable extents of C refertilization
473 brought by incipient deep upper mantle melts (of carbonatitic to kimberlitic affinity[5]), as shown by
474 intermediate C-rich OIBs (e.g., Pico do Fogo and Piton de la Fournaise, Pdf, in the figure).
475
476

Methods

Geological information. The oceanic ridge system displayed in the upper right panel of Fig. 6 is from ref. 51. The crust thickness along the A-B transect is from ref. 52, and the seismicity is from ref. 53.

Volcanic gas dataset. We reviewed available data from the literature and existing catalogues[54-56] to estimate the time-averaged magmatic gas CO_2/S_T ratios for a selection of CR, intraplate OIB, or plume-related MOR (e.g., Iceland[57]) volcanoes. The results are shown in Fig. 2 and 5 and Extended Data Table 1. For previous studies on volcanic arc settings[37,58-59], we only took into consideration high-temperature (>450 °C) fumaroles and/or open-vent crater plumes in which the role of hydrothermal S scrubbing[60-61] can be neglected. In these high-temperature systems, S_T normally corresponds to SO_2 at surface conditions[37]. From an initial screening, only 12 volcanic systems with the above characteristics were identified. Their location is shown in Extended Data Fig. 1 (base map modified from ref. 62). The representativeness of the time-averaged (see Extended Data Table 1 for temporal interval) compositions varies from volcano to volcano, depending on data availability. The magmatic gas CO_2/S_T ratio is especially well constrained at volcanoes where permanent gas monitoring (e.g., Etna[63]) or periodic surveys (e.g., Erebus[64]) have allowed for acquisition of robust time series. In other volcanic systems, the available gas dataset is more limited due to either the remoteness/difficulty of access (e.g., EAR volcanoes) or the lack of persistent high-temperature gas emissions outside eruptions (e.g., Icelandic volcanoes, Pico do Fogo in Cape Verde). Among the EAR volcanoes, Erta Ale in Ethiopia has exhibited a relatively invariant CO_2/S_T ratio composition during (relatively infrequent) observations encompassing 5 decades (1971-2011). In contrast, volcanic gas at Nyiragongo in the Democratic Republic of Congo has evolved towards less CO_2-rich compositions from 1959-1972 (CO_2/S_T of 17.8-22.7) to 2005-2011 (CO_2/S_T of 2.7-6.1), and our large standard derivation around the 1959-2011 average (CO_2/S_T of 11±6.8) reflects this trend (Extended Data Table 1). Nyamuragira gas has only been measured twice to date[65], with rather distinct compositions in 2014 (CO_2/S_T of ~5) and 2015 (CO_2/S_T of ~0.7), implying that the time-

503 averaged composition is poorly constrained for this volcano (2.9±3.1). Similarly, gas observations
504 at Ol Doinyo Lengai have been limited to low-temperature (< 300 °C) fumaroles[66-67] in which the
505 extremely high (>300) CO_2/S_T ratios imply scrubbing of magmatic S from the gas phase. The only
506 exception is represented by the fumarole measurements of ref. 68, for which however only the
507 average CO_2/S_T ratio (~200) of several distinct fumarolic vents (ranging in temperature from 78 to
508 519 °C) is available. As an average that also includes data for low-temperature manifestations, the
509 CO_2/S_T ratio of ~200 certainly overestimates the real magmatic gas signature for the volcano
510 (Extended Data Table 1). Among intraplate volcanoes, Pico do Fogo hosts a fumarolic field in its
511 summit crater with numerous but low-temperature (< 300 °C) vents. Information on magmatic gas
512 chemistry is thus limited to plume observations[69] during the recent 2014-2015 eruption. More
513 abundant gas information is in principle available for Piton de La Fournaise and Kilauea. In the
514 former, however, inter-eruptive gas emissions are very sluggish, while eruptive emissions are
515 logistically challenging to measure from the ground[70]. The only complete analysis of high
516 temperature magmatic gas emissions was obtained during the October 2010 eruption[71]. A vast gas
517 compositional dataset is available for Kilauea[72], but derivation of the characteristic magmatic gas
518 CO_2/S_T ratio for this volcano is problematic because separate (sequential) extraction of CO_2 (below
519 the summit caldera) and SO_2 (as magma laterally intrudes to erupt along the rift zone(s)) makes the
520 CO_2/S_T ratios of summit and rift gases different[73]. The low CO_2/S_T ratio (<1; ref. 72, 74-75)
521 signature of rift-related gases (for which the majority of the data are available) is thus
522 unrepresentative of the parental gas source. The 2008-2018 Halema‘uma‘u summit eruption,
523 although preceded by a surge of CO_2-rich magma supply[76], was similarly associated with the
524 discharge of CO_2-poor gas and magma, implying pre-eruptive CO_2 loss[77]. As such, the early 20th
525 century lava lake gas samples remain the most representative of the parental gas source[73]. The most
526 representative restored gas analyses[78] have CO_2/S_T mass ratios ranging from 1.6 to 5.6, with the
527 latter (sample J8) corresponding to a “quenched equilibrium gas composition”. We use this ratio,
528 corroborated by infrared spectroscopy results[79] for the 1967-68 summit eruption (CO_2/S_T ratio of

5.5), as the most representative of the parental magmatic gas signature at Kilauea. Note that the reconstructed cumulative (summit + rift) CO_2 and SO_2 outputs for 2005-2007 and 2011-2017 (calculated from data in ref. 72, 74-76; ref. 80) lead to CO_2/S_T mass ratio of ~6, very close to our inferred magmatic gas ratio of 5.6.

In addition to the measured compositions, Extended Data Table 1 shows the "predicted" volcanic gas CO_2/S_T ratios for the Ardoukoba, Laki and Nabro volcanoes. The use of predicted rather than measured gas compositions for Ardoukoba is motivated by the very CO_2-poor signature of the latter[81] (Fig. 2), which has been explained as reflecting sampling of a residual, extensively degassed magma source[40,82-83] (sampling was made at the base of the eruptive vent during the final stage of the 1978 fissure eruption). No information on gas chemistry is available for Laki and Nabro, but predicting CO_2/S_T ratios allows quantifying the parental melt CO_2 contents (Fig. 1a) for their 1783-84 (ref. 57) and 2011 (ref. 84) eruptions. In all three cases, the volcanic gas CO_2/S_T ratios are inferred using the gas vs. trace-element best-fit regression equation of Fig. 2a:

$$(CO_2/S_T)_i = 0.35 \cdot \exp(0.03 \cdot (Sr/Sm)_R) \quad (1)$$

where $(Sr/Sm)_R$ is the characteristic Sr/Sm ratio in either primitive MIs or mafic whole-rock samples for each volcano. Errors in the inferred ratios are derived from uncertainty in $(Sr/Sm)_r$ ($\leq$10 %) and in the regression function ($\leq$20 %).

Major and trace-element rock compositions. For each of the 12 volcanoes, we inferred the time-averaged magma composition by selecting the compositions of mafic (SiO_2 < 52 wt%; Extended Data Fig. 2a) whole-rock (WR) samples (see Extended Data Table 1 for data sources). This same methodology has been previously used in arc context[37-38]. The so-obtained trace element compositions, listed in Extended Data Table 2 and illustrated in the chondrite-normalised spider diagram[85] of Extended Data Fig. 2b, are used to calculate the trace element ratios shown in Fig. 2 and 5 (and Extended Data Fig. 3). In these figures, the trace element composition of the DMM is from ref. 18, 86. Since other possible data sources (e.g., MIs) are limited or missing for several volcanoes (see Extended Data Table 1), our use of a set of homogeneous WR-based trace-element

vs. CO_2/S_T populations appears more rigorous. Tests made for volcanoes for which robust WR and MIs are simultaneously available (e.g., Kilauea, Extended Data Fig. 4) demonstrate overlapping trace element ratios for the two datasets and reveal no dependence of trace element ratios on the degree of magma differentiation (at least for SiO_2 <52 wt. % range considered here). This evidence supports the use of averaged WR trace element ratios as representative of parental (primitive) magma composition. The selection of mafic volcanic rocks in our compilation implies that rocks showing typical SiO_2 enrichment owing to crystal fractionation have been excluded when present. For example, data for only basanites and foidites (nephelinites) are averaged in the case of Erebus and Nyiragongo, respectively, while more differentiated magmas (phonolites), and/or immiscibility products (carbonatites), are not considered. Since absolute trace elements abundances vary upon magma differentiation, for the sake of comparison with our inferred parental melt CO_2 contents in Figs. 1b and 1c, we use our best estimates of Nb and Ba concentrations in parental magmas (Extended Data Table 2), obtained by averaging the composition of the most primitive (SiO_2-poor and Mg-rich) WR/MIs (see Extended Data Fig. 4 for the Kilauea example).

Calculation of the mantle melting fraction. For each volcano, we estimated the mantle source partial melting degrees F, required to convert parental melt CO_2 contents into source mantle C (and to generate the chosen primitive whole-rock compositions), by applying a nonmodal batch melting equation[87]. We solve the equation, expressed as:

$$C_L = C_0/[D + F\times(1-P)] \quad (2)$$

using the concentration of a selected incompatible element (Zr) in the most primitive magma of each volcano. In equation 2, C_L is the Zr concentration in the magma, and C_0 the Zr concentration in the mantle source. P is the partition coefficient of the element weighted for the eutectic mineral melting proportions, and D is the partition coefficient weighted for the modal composition of the mantle source. To obtain results comparable between each of the selected case studies and avoid any possible dependency on modal composition of the mantle source/s and/or the mineral proportions involved during melting, we assumed almost totally incompatible Zr behaviour. Such

581 an assumption results in the approximation of P and D to zero, thus simplifying equation 2 into C_L
582 = C_0/F. In this way, the partial melting degree of the mantle sources beneath each volcano can be
583 approximated as the ratio between the Zr concentrations in the source and the primitive magma ($F = C_0/C_L$).
584 Well aware that the dependency of this method is mostly on the concentration of Zr in the
585 mantle source, we conservatively calculated the partial melting degree from each primitive magma
586 composition by taking into account two different mantle source end-members, i.e. the primitive
587 mantle (PM; ref. 85), with a C_{Zr} of 11.2 ppm, and an enriched mantle (EM) analogous to that
588 proposed by ref. 88, with a C_{Zr} of 20 ppm (Extended Data Table 2). The "enriched" nature of the
589 studied magmas (Figs. 2-5 and Extended Data Fig. 2) would result in unrealistically low (0.01-0.06)
590 degrees of partial melting if a DMM end-member was considered. Our inferred F values are listed
591 (for both the considered PM and EM sources) in Extended Data Table 3. For each locality, we
592 select the most correct F solution from the scrutiny of available knowledge, e.g., existing literature
593 constraints on a PM/EM being implicated. Our F values are in good agreement with those
594 previously estimated at each locality (Extended Data Table 3).
595 **Calculation of the depth/pressure of melting initiation.** The pressure of partial melting (plotted
596 in Fig. 3) was calculated using a T-dependent, H_2O-independent barometer[89] (equation 42) applied
597 to the most primitive WR compositions from the selected volcanoes. This barometer considers the P
598 dependencies[90] of the melt silica activity, and was calibrated over a range of P, T and SiO_2
599 conditions (of respectively 0.0001-7 GPa, 825-2000°C and 31.5-70 wt.%) using a global dataset of
600 experimental partial melts. The T inputs for the barometer are the liquidus temperatures of the
601 selected primitive magmas, calculated using the Rhyolite-MELTS code[91]. To retrieve liquidus T,
602 we also consider (Extended Data Table 2) the most undegassed H_2O and CO_2 concentrations
603 reported on MIs for each of the studied magmatic suites (data-source, see Extended Data Table 1).
604 We stress a lack of interdependencies between thermometric and barometric equations, i.e., between
605 T and P and/or partial melting degree[92]. The same PT function[89] was also used to infer
606 depths/pressures of mantle melting initiation for the MOR segments[20] shown in Fig. 3. At this aim,

607 we used the segment-averaged potential temperatures, calculated from average ridge depths[20] and
608 the depth-temperature relationship inferred by ref. 93. The source mantle (DMM) C contents were
609 estimated[20] from MOR segment-averaged Ba contents[94], assuming a uniform CO_2/Ba mantle ratio
610 of 81. For comparison, the pressures of initiation of melting, previously inferred for our case study
611 volcanoes with a variety of geobarometric methods, are also listed in Extended Data Table 3. As an
612 example, according to recent petrogenetic models[95-96], the parental olivine melilititic magmas at
613 Nyiragongo are generated by small-fraction partial melting of a garnet- and phlogopite-bearing
614 mantle source generated by carbonate metasomatism[97]. This mantle mineral assemblage, in view of
615 experimental results on P-T conditions of peridotite melting[98], is consistent with melting depths of
616 80 (Nyamuragira) to 150 (Nyiragongo) km (ref. 97). Such depth values and associated partial
617 melting degrees are very close to those (82 and 150 km; Fs, of 7.9 and 5 %; Extended Data Table 3)
618 estimated in our study.

619 **Calculation of the trace element signature of the metasomatic agent**. The trace element
620 compositions of the endmember metasomatic C-rich melts (mCm) (Extended Data Table 4) are
621 obtained from data regression to the (CO_2/S_T) vs. trace element data. Our melting-mixing procedure
622 is illustrated in Extended Data Fig. 6 for the Sr/Sm example (an automatic calculation routine,
623 developed in R code, was applied interactively to a sequence of couples of trace element ratios). We
624 initially use the batch melting equation[87] to calculate the $(CO_2/S_T)_M$ and $(Sr/Sm)_M$ ratios of the
625 mantle source(s) from the original volcanic gas $(CO_2/S_T)_G$ and rock $(Sr/Sm)_R$ datasets (Extended
626 Data Fig. 6):

627 $$(CO_2/S_T)_M=(CO_2/S_T)_G\cdot[(Kd_C\cdot(1-F)+F)/(Kd_S\cdot(1-F)+F)] \quad (3)$$

628 $$(Sr/Sm)_M=(Sr/Sm)_R\cdot[(Kd_{Sr}\cdot(1-F)+F)/(Kd_{Sm}\cdot(1-F)+F)] \quad (4)$$

629 Calculations are performed for a set of melting fractions F (0.025, 0.5, 0.1, 0.2) covering the range
630 of mantle melting conditions at the studied volcanoes (Extended Data Table 3). In the calculations,
631 we use the trace element Kd values of C = 0.00055, S = 0.079, Sr = 0.025, and Sm = 0.045.

The generated $(CO_2/S_T)_M$ and $(Sr/Sm)_M$ populations (one for each F value; Extended Data Fig. 6) are then fitted using an R-written routine[99] by a best-fit mixing equation[100]:

$$(Sr/Sm)_M = -((S_{DMM}\cdot Sr_{mCm}-S_{mCm}\cdot Sr_{DMM})\cdot(CO_2/S_T)_M+ (Sr_{DMM}\cdot C_{mCm}-Sr_{mCm}\cdot C_{DMM}))/$$

$$((Sm_{DMM}\cdot S_{mCm}-Sm_{mCm} *S_{DMM}) \cdot(CO_2/S_T)_M+ (Sm_{mCm}\cdot C_{DMM}-Sm_{DMM}*C_{mCm})) \quad (5)$$

where $(CO_2/S_T)_{DMM}$ and $(Sr/Sm)_{DMM}$ refer to the characteristic ratios in the depleted MORB mantle (DMM), and $(CO_2/S_T)_{mCm}$ and $(Sr/Sm)_{mCm}$ stand for the characteristic compositions of the metasomatic C-rich melts (mCm). From experimental and petrological evidence[6], we assume the most common mantle metasomatic agents are C-rich melts formed via incipient melting of either carbonated peridotites[4-5] and/or subducted carbonated oceanic crust[101-102].

To solve equation 5, the C, S and Sr concentrations of the DMM are fixed averaging published results[1,2,18,86], while those of the mCm are based on the composition of natural kimberlitic and carbonatitic rocks and/or experimental melts formed during mantle rock melting expertiments[4-6] (see below). With a set of assigned C, S, and Sr values, the algorithm iteratively determines the nonlinear least-squares estimate of the Sm concentrations of both DMM and mCm. This operation, repeated interactively for a sequence of trace element ratios, allows deriving the whole trace element composition suite of the mCm (Extended Data Table 4 and Fig. 5c).

Experiments[4-6,98] demonstrate that incipient mantle melts form a continuous trend from carbonatitic to carbonated silicate (kimberlite-like) melts, and we therefore consider 5 distinct scenarios (models Cb1, Cb2, Kb1, Kb2, and Kb3) to cover this possible range. In the Cb1 and Cb2 models (Extended Data Table 4), we assume a mCm with the most CO_2-enriched (40 wt%) compositions, those of natural (Fig. 4) and experimental (Extended Data Fig. 5) carbonatitic melts. Synthetic carbonatitic liquids (< 10 wt% SiO_2; Extended Data Fig. 5) formed by melting of carbonated peridotites and eclogites[5,102] are mostly dolomitic, implying that they do possess the Sr-rich compositional signature (Fig. 4) required to explain our volcanic gas-trace-element associations (Figs. 2,5). We select two "carbonatitic" model scenarios (Cb1 and Cb2) to explore the effect of Sr on our results, in which the mCm Sr content is fixed at either 14,000 ppm (that of the most calcic natural

carbonatites; Cb1) or at 4,500 ppm (Cb2). The latter value is inferred using the Sr vs. CO_2 correlation we identify using our reconstructed parental melt CO_2 for plume (MOR/OIB) and CR volcanoes (e.g., from extrapolating this correlation at 40 wt% CO_2) (Fig. 4).

Natural (erupted) kimberlitic rocks have compositional signatures controlled by extents of degassing, assimilation (of mantle and crustal rocks) and alteration[103], and are thus unrepresentative of primary melt compositions. Nevertheless, they arguably represent the best proxy for the carbonated silicate melts rising from deep in the convecting mantle[104]. Other related ultrabasic rocks, such as lamproites and lamprophyres, are typically less CO_2-rich and exhibit more radiogenic isotope compositions, reflecting a shallower derivation in the Sub Continental Lithospheric Mantle[104-105]. The GeoRoc CO_2 average of 7 wt% for natural erupted kimberlites is considered[104] to represent a lower range for their parental mantle melt CO_2 contents, owing to extensive (>10 wt%; ref. 102) degassing prior to/during surface emplacement. In our "kimberlitic" simulation scenarios, we therefore assume CO_2 contents of either 20 wt% (ref. 104) (Kb1 simulation) or 7 wt% (Kb2 and Kb3 simulations). The Sr contents of the Kb models (Extended Data Table 4) are inferred (as above) from our Sr vs. parental CO_2 correlation (Fig. 4).

Our mCm are assumed to have relatively low S concentrations (1000 mg/kg for Cb1, Cb2, Kb1, and Kb2). This is inferred from experimentally derived sulfur concentrations at sulfide saturation (SCSS) (Extended Data Fig. 5) that imply limited S transport capacity of carbonatitic to carbonated silicate melts below continents and oceans[106]. A 1000 ppm S mCm is also the GeoRoc average for kimberlitic-carbonatitic natural rocks (Extended Data Fig. 5). Experiments[106] suggest a positive dependence of SCSS on SiO_2 melt content (Extended Data Fig. 5), and we assume 2000 ppm S in Kb3 model to explore the possible effect of this dependence (Extended Data Table 4).

One critical aspect is that while our inferred absolute trace element mCm compositions vary in between the 5 model scenarios (Extended Data Table 4), the trace element ratios we derive are more uniform (Figs. 1,4b). This evidence implies that the relative trace elements proportions are more strictly determined by the fitted compositional volcano trends than by the assumed composition of

684 the metasomatic agent (mCm) we use for the fitting. The spider diagram of Fig. 5c demonstrates
685 this and shows that the primitive mantle (PM)-normalised Cb1 and Kb1 trends are very similar and
686 only shifted vertically. The Cb1 and Kb1 PM-normalised trends overlap the composition of natural
687 kimberlites, while they lack the strong Ta, Zr and Hf negative peaks of natural carbonatites. Our
688 mCms thus point to a metasomatic agent more affine to a carbonated silicate melt, rather than to a
689 carbonatite.
690
691
692 **Methods references**

693 51. Commission for the Geological Map of the World (CGMW) Geological map of the world,
694 scale 1:25,000,000, U.N. Educ. Sci. and Cult. Org., Paris (2000).

695 52. Laske, G., Masters., G., Ma, Z., and Pasyanos, M., Update on CRUST1.0 - A 1-degree Global
696 Model of Earth's Crust, Geophys. Res. Abstracts, 15, Abstract EGU2013-2658 (2013).

697 53. Ekström, G., Nettles, M. & Dziewonski, A. M. The global CMT project 2004 −2010:
698 centroid-moment tensors for 13,017 earthquakes. Phys. Earth Planet. Inter. 200,1–9 (2012).

699 54. Symonds, R.B., Rose, W.I., Bluth, G.J.S., Gerlach, T.M. Volcanic-gas studies: methods,
700 results and applications, *Rev. Mineral*. **30**, 1-66 (1994).

701 55. Oppenheimer, C., Fischer, T.P. & Scaillet B. Volcanic Degassing: Process and Impact. In
702 Treatise on Geochemistry, The Crust, (eds. Holland, H.D. and Turekian, K.K.). Elsevier,
703 Second Edition 4, 111-179 (2014).

704 56. Fischer, T.P., & Chiodini, G. Volcanic, Magmatic and Hydrothermal Gas Discharges. In
705 Encyclopaedia of Volcanoes, 2nd Edition, 779-797 http://dx.doi.org/10.1016/B978-0-12-
706 385938-9.00045-6 (2015).

57. Hartley, M.E., Maclennan, J., Edmonds, M., & Thordarson, T., Reconstructing the deep CO2 degassing behaviour of large basaltic fissure eruptions. Earth Planet. Sci. Lett. 393, 120–131 (2014).

58. Fischer, T.P. Fluxes of volatiles (H_2O, CO_2, N_2, Cl, F) from arc volcanoes. *Geochemical Journal*, **42** (1), 21-38 (2008).

59. Wallace, P.J. Volatiles in subduction zone magmas: concentrations and fluxes based on melt inclusions and volcanic gas data. *J. Volcanol. Geotherm. Res*. **140**, 217-240 (2005).

60. Symonds, R.B., Gerlach, T.M., Reed, M.H. Magmatic gas scrubbing: implications for volcano monitoring. *J. Volcanol. Geotherm. Res*. **108**, 303-341 (2001).

61. Di Napoli, R., Aiuppa, A., Bergsson, B., et al. Reaction path models of magmatic gas scrubbing. *Chem. Geol*., **420**, 251-269 (2016).

62. Smith, W.H.F. & Sandwell, D.T. Global seafloor topography from satellite altimetry and ship depth soundings. *Science* **277**, 1957-1962 (1997).

63. Aiuppa, A., Giudice, G., Liuzzo, M. (2017a). Volcanic gas plume data from Etna Volcano (Italy), Version 1.0. Interdisciplinary Earth Data Alliance (IEDA). https://doi.org/10.1594/IEDA/100643.

64. Ilanko, T. Geochemistry of gas emissions from Erebus volcano, Antarctica, PhD Dissertation, Cambridge University (2014).

65. Bobrowski, N., et al., Plume composition and volatile flux of Nyamulagira volcano, Democratic Republic of Congo, during birth and evolution of the lava lake, 2014–2015. *Bulletin of Volcanology* **79**:90, https://doi.org/10.1007/s00445-017-1174 (2017)

66. Koepenick KW, Brantley SL, Thompson JM, Rowe GL, Nyblade AA, Moshy C. Volatile emissions from the crater and flank of Oldoinyo Lengai volcano, Tanzania. J Geophys Res 1996;101:13819–30.

67. Oppenheimer, C., Burton, M.R., Durieux, J., & Pyle, D.M. Open-path Fourier transform spectroscopy of gas emissions from Oldoinyo Lengai volcano, Tanzania. *Optics and Lasers in Engineering* **37**, 203–214 (2002)

68. Javoy M, Pineau F, Cheminee JL, Krafft M. The gas magma relationship in the 1988 eruption of Oldoinyo Lengai (Tanzania), Abstract, EOS. Trans Am Geophys Union 1998, 69:1466 (1988).

69. Hernández, P.A., et al. Chemical composition of volcanic gases emitted during the 2014-15 Fogo eruption, Cape Verde, Geophysical Research Abstracts, Vol. 17, EGU2015-9577, 2015, EGU General Assembly 2015 (2015)

70. Di Muro, A., Métrich, N., Allard, P., Aiuppa, A., Burton, M., Galle, B., & Staudacher, T., Magma Degassing at Piton de la Fournaise Volcano. In: P. Bachèlery et al. (eds.), Active Volcanoes of the Southwest Indian Ocean, Active Volcanoes of the World, Springer-Verlag Berlin Heidelberg. doi 10.1007/978-3-642-31395-0_12 (2016)

71. Allard, P., et al., First measurements of magmatic gas composition and fluxes during an eruption (October 2010) of Piton de la Fournaise hot spot volcano, La Reunion island. Geophysical Research Abstracts 13, abstract n. EGU2011-13182, EGU General Assembly (2011)

72. Sutton, A. J. & Elias, T. One hundred volatile years of volcanic gas studies at the Hawaiian Volcano Observatory. In: Characteristics of Hawaiian Volcanoes. US Geological Survey Professional Paper 1801 (eds. M. P. Poland, T. J. Takahashi & C. M. Landowski), 295–320 (USGS) (2014)

73. Gerlach, T. M., & Graeber E. J. Volatile budget of Kilauea Volcano, *Nature*, **313**, 273–277(1985)

74. Edmonds M. and Gerlach T. M. Vapor segregation and loss in basaltic melts. *Geology* **35**, 751–754 (2007).

75. Elias T, Kern C, Horton KA, Sutton AJ and Garbeil H (2018) Measuring SO_2 Emission Rates at Kılauea Volcano, Hawaii, Using an Array of Upward-Looking UV Spectrometers, 2014–2017. Front. Earth Sci. 6:214. doi: 10.3389/feart.2018.00214

76. Poland, M. P., Miklius, A., J. Sutton, A. & Thornber, C. R. A mantle-driven surge in magma supply to Kilauea Volcano during 2003-2007. *Nat. Geosci*. **5**, 295-300 (2012).

77. Edmonds, M., et al Magma storage, transport and degassing during the 2008–10 summit eruption at Kılauea Volcano, Hawai‘i. *Geochim. Cosmochim. Acta*, **123**, 284-301 (2013).

78. Gerlach, T.M. Evaluation of volcanic gas analyses from Kilauea volcano, *J. Volcanol. Geotherm. Res.* 7, 295-317 (1980).

79. Naughton, J.J., Derby, J.V., & Glover, R.B. Infrared measurements on volcanic gas and fume: Kilauea eruption, 1968. *J. Geophys. Res*., **74**, 3273–3277 (1969**)**

80. Werner C., (2019), personal communication

81. Allard, P., Tazieff, H., Dajlevic, D. Observations of seafloor spreading in Afar during the November 1978 fissure eruption. *Nature,* **279**, 30-33 (1979).

82. Gerlach, T.M. Restoration of new volcanic gas analyses from basalts of the Afar region: further evidence of CO_2 degassing trends. *J. Volcanol. Geotherm. Res*. **10**, 83-91 (1981).

83. Gerlach, T.M., Investigation of volcanic gas analyses and magma outgassing from Erta 'Ale lava lake, Afar, Ethiopia. *Journal Volcanol. ì Geotherm. Res.* **7**, (3–4), 415–441 (1980).

84. Donovan, A., Blundy, J., Oppenheimer, C., Buisman, I. The 2011 eruption of Nabro volcano, Eritrea: perspectives on magmatic processes from melt inclusions. *Contributions to Mineralogy and Petrology* **173**:1 https://doi.org/10.1007/s00410-017-1425-2 (2018)

85. Sun, S.S, & McDonough, W.F. Chemical and isotopic systematics of oceanic basalts: implications for mantle composition and processes, in: A.D. Saunders, M.J. Norry (Eds.), Magmatism in the Ocean Basins, Geological Society, London, 313– 345 (1989).

86. Workman, R.K., & Hart, S.R. Major and trace element composition of the depleted MORB mantle (DMM). *Earth Planet. Sci. Lett.* **231**, 53-7 (2005).

87. Shaw, D.M. Trace element melting models. *Physics and Chemistry of the Earth*, **11**, 577-586 (1979)

88. Casetta, F., Giacomoni, P. P., Ferlito, C., Bonadiman, C., & Coltorti, M. The evolution of the mantle source beneath Mt. Etna (Sicily, Italy): from the 600 ka tholeiites to the recent trachybasaltic magmas. *International Geology Review*, **62**(3), 338-359 (2020).

89. Putirka, K.D., Thermometers and Barometers for Volcanic Systems, *Rev. Mineral. Geochem*., **69** (1), 61–120 (2008).

90. Beattie, P. Olivine-melt and orthopyroxene-melt equilibria. *Contributions to Mineralogy and Petrology*, **115**(1), 103-111 (1993).

91. Gualda, G.A.R., Ghiorso, M.S., Lemons, R.V., Carley, T.L. Rhyolite-MELTS: a Modified Calibration of MELTS Optimized for Silica-rich, Fluid-bearing Magmatic Systems. *J. Petrol*., **53**, 5, 875–890, https://doi.org/10.1093/petrology/egr080 (2012).

92. Putirka, K. D. Mantle potential temperatures at Hawaii, Iceland, and the mid-ocean ridge system, as inferred from olivine phenocrysts: Evidence for thermally driven mantle plumes. *Geochemistry, Geophysics, Geosystems*, **6**(5), 1-14 (2005).

93. Dalton, C. A., Langmuir, C. H., & Gale, A. Geophysical and geochemical evidence for deep temperature variations beneath midocean ridges. *Science*, **344**, 80–83 (2014).

94. Gale, A., Langmuir, C.H., & Dalton, C.A., The global systematics of ocean ridge basalts and their origin. *J. Petrol*. **55**, 1051–1082 (2014).

95. Demant, A., Lestrade, P., Lubala, R.T., Kampunzu, A.B., & Durieux, J. Volcanological and petrological evolution of Nyiaragongo Volcano, Virunga volcanic field, Zaire. *Bull. Volcanol*. **56** (1), 47–61 (1994)

96. Platz, T., Foley, S.F., & Andre, L. Low-pressure fractionation of the Nyiragongo volcanic rocks, Virunga Province, D. R. Congo. *J. Volcanol. Geotherm. Res*. **136**, 269–295 (2004).

97. Chakrabarti, R., Basu, A.R., Santo, A.P., Tedesco, D., Vaselli, O. Isotopic and geochemical evidence for a heterogeneous mantle plume origin of the Virunga volcanics, Western rift, East African Rift system, *Chemical Geology* **259**, 273–289 (2009)

98. Foley, S. F. et al. The composition of near-solidus melts of peridotite in the presence of CO_2 and H_2O at 40–60 kbar. *Lithos* **112S**, 274–283 (2009).

99. Janousek, V., Moyen, J.-F., Martin, H., Erban, V., Farrow, C. Geochemical Modelling of Igneous Processes – Principles And Recipes in R Language. Springer Geochemistry, Springer (2015)

100. Langmuir CH, Vocke RD, Hanson GN A general mixing equation with application to Icelandic basalts. *Earth Planet Sci Lett* **37**:380–392 (1978)

101. Thomson A. R., Walter M. J., Kohn S. C. & Brooker R. A. Slab melting as a barrier to deep carbon subduction. *Nature* **529** (7584), 76–79. https://doi.org/10.1038/nature16174 (2016).

102. Sun C., & Dasgupta R. Slab–mantle interaction, carbon transport, and kimberlite generation in the deep upper mantle. Earth Planet. Sci. Lett. 506, 38–52 (2019).

103. Mitchell, R.H., Giuliani, A., & O'Brien, H. What is a Kimberlite? Petrology and Mineralogy of Hypabyssal Kimberlites. *Elements* **15**, 381–386 (2019)

104. Pearson, D.G., Woodhead, J., & Janney P.E. Kimberlites as Geochemical Probes of Earth's Mantle, *Elements* **15**, 387–39 (2019)

105. Casetta, F., Ickert, R. B., Mark, D. F., Bonadiman, C., Giacomoni, P. P., Ntaflos, T., & Coltorti, M. The alkaline lamprophyres of the Dolomitic Area (Southern Alps, Italy): markers of the Late Triassic change from orogenic-like to anorogenic magmatism. *Journal of Petrology*, **60**(6), 1263-1298 (2019).

106. Chowdhury, P., Dasgupta, R., Sulfur extraction via carbonated melts from sulfide-bearing mantle lithologies – Implications for deep sulfur cycle and mantle redox. *Geochim. Cosmochim. Acta* **269**, 376–397 (2020)

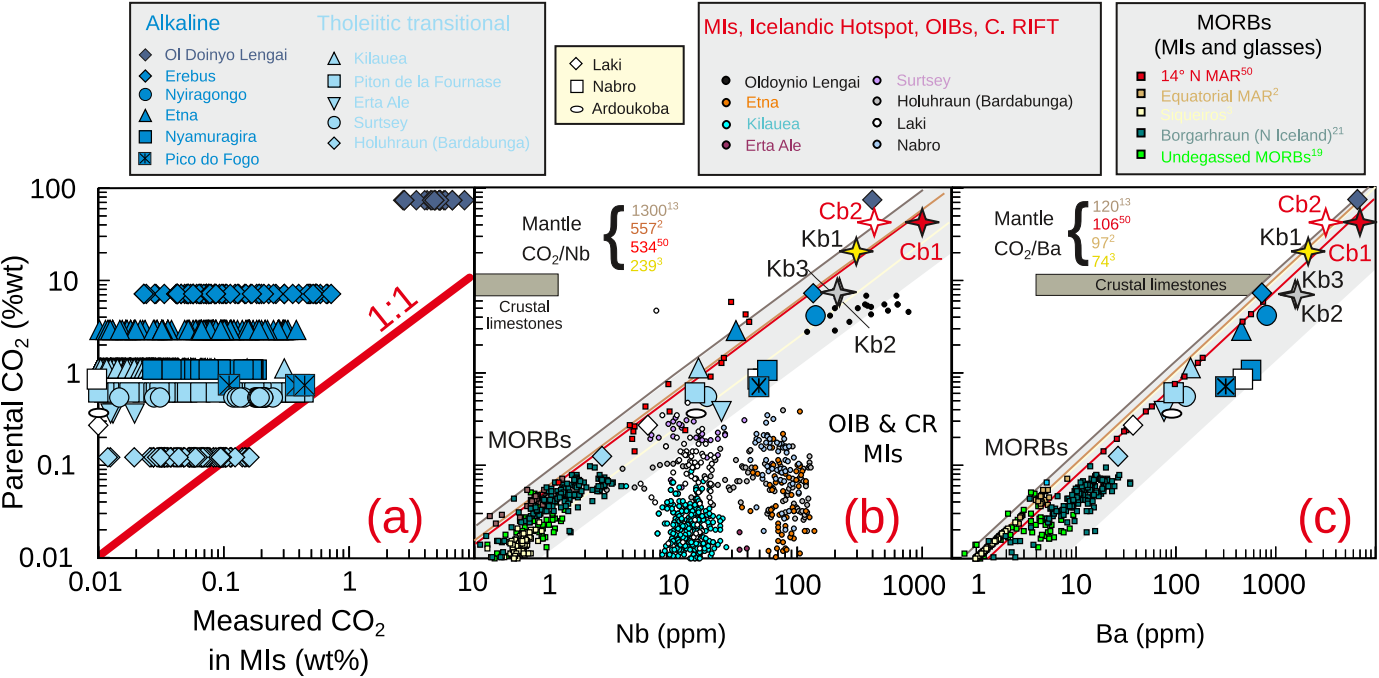
Alkaline
Ol Doinyo Lengai
Erebus
Nyiragongo
Etna
Nyamuragira
Pico do Fogo
Tholeiitic transitional
Kilauea
Piton de la Fournase
Erta Ale
Surtsey
Holuhraun (Bardabunga)
Laki
Nabro
Ardoukoba
MIs, Icelandic Hotspot, OIBs, C. RIFT
Oldoynio Lengai
Etna
Kilauea
Erta Ale
Surtsey
Holuhraun (Bardabunga)
Laki
Nabro
MORBs
(MIs and glasses)
14° N MAR[50]
Equatorial MAR[2]
Siqueiros
Borgarhraun (N Iceland)[21]
Undegassed MORBs[19]
Parental CO2 (%wt)
100
10
1
0.1
0.01
1:1
Measured CO2
in MIs (wt%)
(a)
Mantle
CO2/Nb
1300[13]
557[2]
534[50]
239[3]
Crustal
limestones
Cb2
Kb1
Cb1
Kb3
Kb2
MORBs
OIB & CR
MIs
(b)
Nb (ppm)
Mantle
CO2/Ba
120[13]
106[50]
97[2]
74[3]
Crustal limestones
Cb2
Kb1
Cb1
Kb3
Kb2
MORBs
(c)
Ba (ppm)

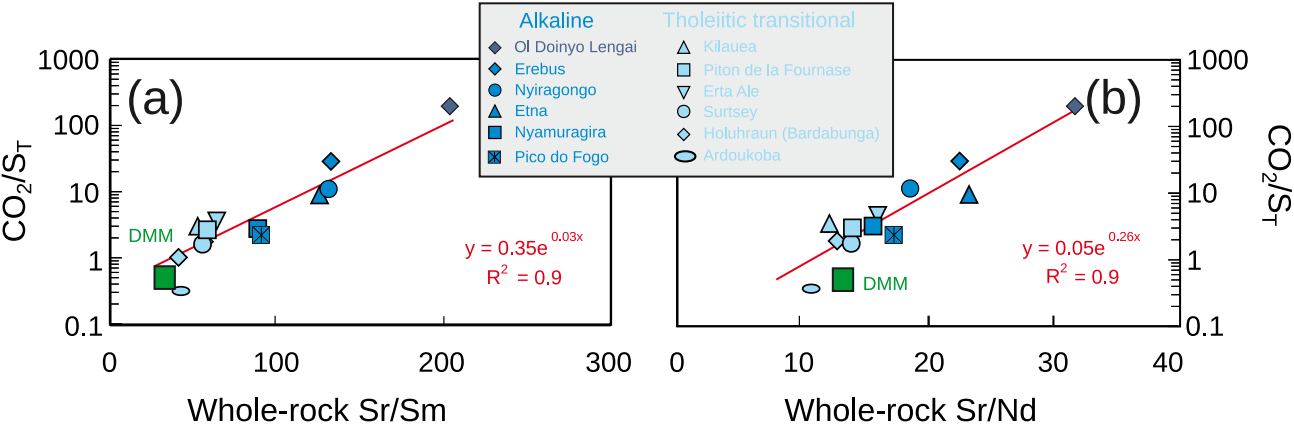
Alkaline
Ol Doinyo Lengai
Erebus
Nyiragongo
Etna
Nyamuragira
Pico do Fogo
Tholeiitic transitional
Kilauea
Piton de la Fournase
Erta Ale
Surtsey
Holuhraun (Bardabunga)
Ardoukoba
(a)
(b)
DMM
DMM
y = 0.35e^0.03x
R^2 = 0.9
y = 0.05e^0.26x
R^2 = 0.9
CO2/ST
CO2/ST
1000
100
10
1
0.1
0
100
200
300
0
10
20
30
40
Whole-rock Sr/Sm
Whole-rock Sr/Nd

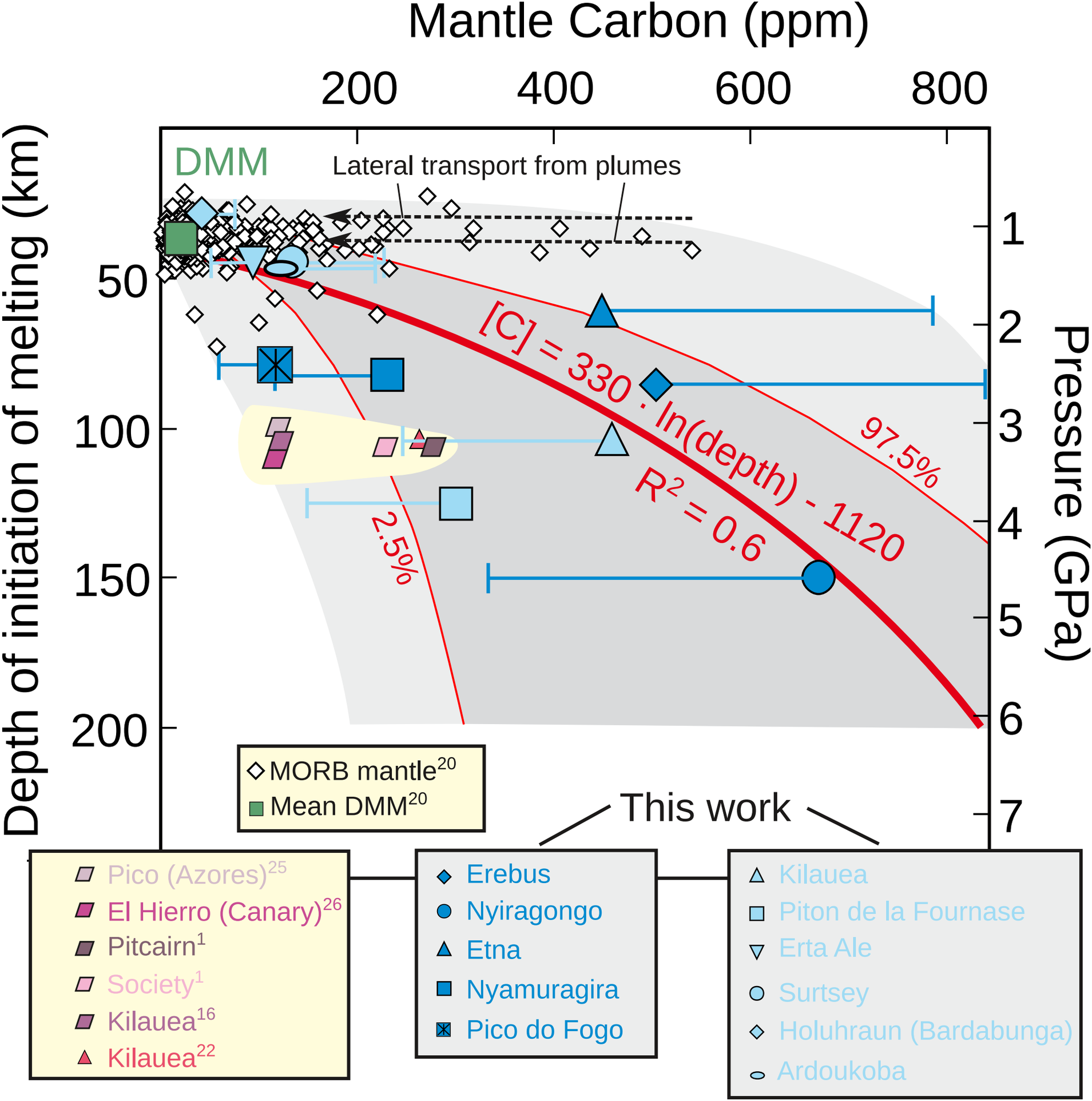
Mantle Carbon (ppm)
200
400
600
800
DMM
Lateral transport from plumes
[C] = 330 . ln(depth) - 1120
R² = 0.6
97.5%
2.5%
Depth of initiation of melting (km)
50
100
150
200
Pressure (GPa)
1
2
3
4
5
6
7
MORB mantle[20]
Mean DMM[20]
This work
Pico (Azores)[25]
El Hierro (Canary)[26]
Pitcairn[1]
Society[1]
Kilauea[16]
Kilauea[22]
Erebus
Nyiragongo
Etna
Nyamuragira
Pico do Fogo
Kilauea
Piton de la Fournase
Erta Ale
Surtsey
Holuhraun (Bardabunga)
Ardoukoba

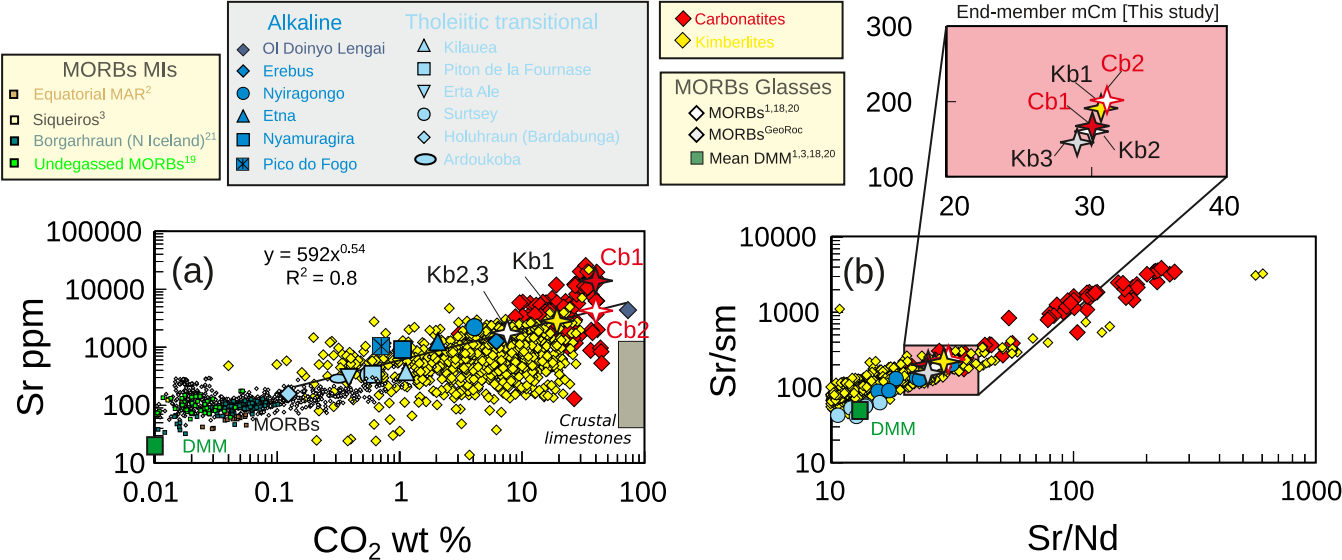
MORBs MIs
Equatorial MAR[2]
Siqueiros[3]
Borgarhraun (N Iceland)[21]
Undegassed MORBs[19]
Alkaline
Ol Doinyo Lengai
Erebus
Nyiragongo
Etna
Nyamuragira
Pico do Fogo
Tholeiitic transitional
Kilauea
Piton de la Fournase
Erta Ale
Surtsey
Holuhraun (Bardabunga)
Ardoukoba
Carbonatites
Kimberlites
MORBs Glasses
MORBs[1,18,20]
MORBsGeoRoc
Mean DMM[1,3,18,20]
End-member mCm [This study]
Kb1
Cb2
Cb1
Kb3
Kb2
(a)
y = 592x^0.54
R² = 0.8
Kb2,3
Kb1
Cb1
Cb2
MORBs
DMM
Crustal limestones
Sr ppm
CO2 wt %
(b)
Sr/sm
Sr/Nd
DMM

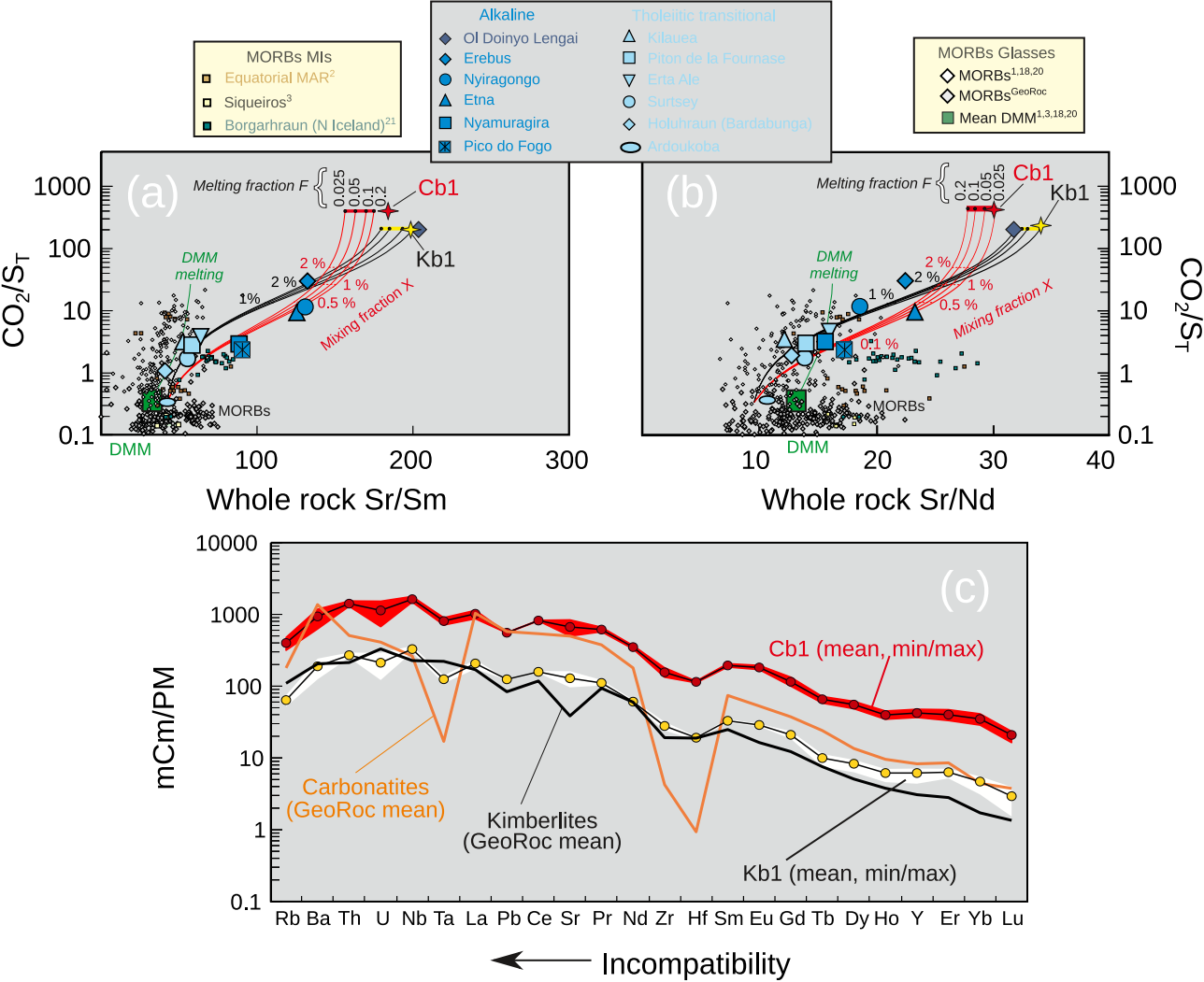
Alkaline
Ol Doinyo Lengai
Erebus
Nyiragongo
Etna
Nyamuragira
Pico do Fogo
Tholeiitic transitional
Kilauea
Piton de la Fournase
Erta Ale
Surtsey
Holuhraun (Bardabunga)
Ardoukoba
MORBs MIs
Equatorial MAR[2]
Siqueiros[3]
Borgarhraun (N Iceland)[21]
MORBs Glasses
MORBs[1,18,20]
MORBs[GeoRoc]
Mean DMM[1,3,18,20]
(a)
Melting fraction F
0.025
0.05
0.1
0.2
Cb1
Kb1
DMM melting
2 %
2 %
1%
1 %
0.5 %
Mixing fraction X
MORBs
DMM
CO2/ST
Whole rock Sr/Sm
(b)
Melting fraction F
0.2
0.1
0.05
0.025
Cb1
Kb1
DMM melting
2 %
2 %
1 %
0.5 %
Mixing fraction X
0.1 %
MORBs
DMM
CO2/ST
Whole rock Sr/Nd
(c)
mCm/PM
Cb1 (mean, min/max)
Carbonatites (GeoRoc mean)
Kimberlites (GeoRoc mean)
Kb1 (mean, min/max)
Rb Ba Th U Nb Ta La Pb Ce Sr Pr Nd Zr Hf Sm Eu Gd Tb Dy Ho Y Er Yb Lu
Incompatibility

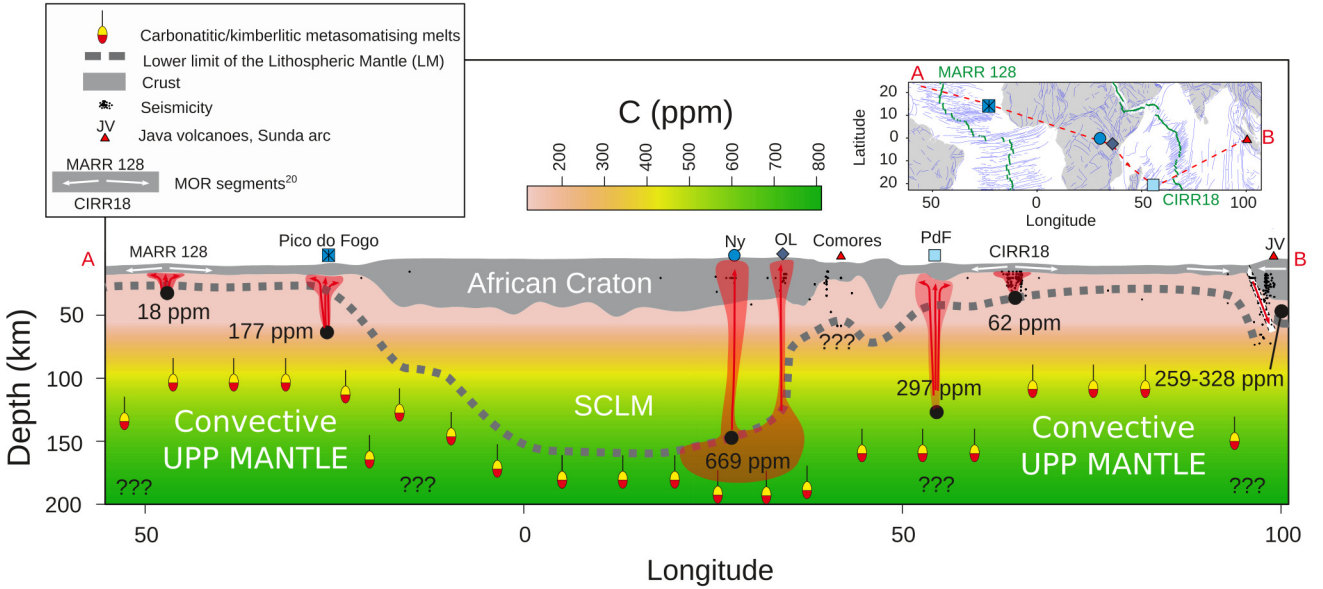
Carbonatitic/kimberlitic metasomatising melts
Lower limit of the Lithospheric Mantle (LM)
Crust
Seismicity
JV
Java volcanoes, Sunda arc
MARR 128
CIRR18
MOR segments[20]
C (ppm)
200
300
400
500
600
700
800
A
B
MARR 128
CIRR18
Latitude
Longitude
Pico do Fogo
Ny
OL
Comores
PdF
JV
African Craton
18 ppm
177 ppm
62 ppm
???
297 ppm
259-328 ppm
669 ppm
SCLM
Convective
UPP MANTLE
Convective
UPP MANTLE
Depth (km)
Longitude